Chinese Chemical Letters 35 (2024) 109501

Contents lists available at ScienceDirect

Chinese Chemical Letters

journal homepage: www.elsevier.com/locate/cclet

Ultrafast synthesis of nanocrystalline spinel oxides by Joule-heating method

Wenxuan Yang, Long Shang, Xiaomeng Liu, Sihan Zhang, Haixia Li*, Zhenhua Yan*, Jun Chen

State Key Laboratory of Advanced Chemical Power Sources, Key Laboratory of Advanced Energy Materials Chemistry (Ministry of Education), Frontiers Science Center for New Organic Matter, College of Chemistry, Nankai University, Tianjin 300071, China

ARTICLE INFO

Article history:
Received 29 November 2023
Revised 23 December 2023
Accepted 4 January 2024
Available online 6 January 2024

Keywords:
Ultrafast synthesis
Spinel oxides
Joule-heating
In-situ TEM
Oxygen reduction

ABSTRACT

Spinel oxides, with the formula AB_2O_4 (A and B represent metal ions) perform superior electrocatalytic characteristic when A and B are transition metals like Co, Fe, Mn, *etc*. Abundant researches have been attached to the structure designments while methods are often energy-intensive and inefficient. Here, we devised a universal strategy to achieve rapid synthesis of nanocrystalline spinel materials with multiple components (Co_3O_4, Mn_3O_4, $CoMn_2O_4$ and $CoFe_2O_4$ are as examples), where phase formation is within 15 s. Under the Joule-heating shock, a crack-break process of microcosmic phase transformation is observed by *in-situ* transmission electron microscopy. The half-wave potential values of Co_3O_4–JH, Mn_3O_4–JH, $CoMn_2O_4$–JH and $CoFe_2O_4$–JH in the electrocatalytic oxygen reduction reaction were 0.77, 0.78, 0.79 and 0.76, respectively. This suggests that the Joule heating is a fast and efficient method for the preparation of spinel oxide electrocatalysts.

Spinel oxides, generally with the formula AB_2O_4 (where A and B are metal ions), have been extensively studied for their various physical or chemical properties, such as magnetism, electrical conductivity, optical properties and catalytic activity [1–3] caused by diverse compositions [4], micro/nano structures [5,6], electron configurations [7,8] and valence states [9]. The electrical characteristic and redox reactivity due to their variable valence states of spinel oxides make them capable to play a role in the applications of energy conversion and storage systems, such as $LiMn_2O_4$ and $LiNi_{0.5}Mn_{1.5}O_4$ for cathode materials of Li-ion batteries [10,11] and $NiCo_2O_4$ for supercapacitors [12]. In the field of electrocatalysis, spinel oxides are considered as a competitive alternative to noble metal-based catalysts (*e.g.*, Pt/C) because of their high oxygen reduction reaction (ORR) catalytic activity and low cost, which are used in fuel cells [13,14] and metal-air batteries [15,16]. Transition metals like Co, Mn and Fe are the most common components in such spinel type electrocatalysts [17].

Lower time cost, lower energy cost and higher volume synthesis methods for metal oxides catalysts have been pursued [18]. Although spinel oxides have a significant advantage in terms of cost compared to commercial noble metal-based catalysts, approaches utilized to prepare them become an obstacle in the way to commercialization. A direct high temperature solid phase method is an ordinary means which is beneficial to get a pure phase with good crystallization, while it requires a high temperature for a long duration of reaction for phase formation and crystallization, causing a high time cost and low energy efficiency [19]. Hydrothermal is also a common technique for preparing products with high dispersion and small particle size, but it is not feasible for a mass production [20]. Some vapor phase methods such as vapor deposition and spraying are more technically demanding and only a small amount of product can be synthesized in a single batch [21]. Traditional synthesis methods are either time-consuming and energy consuming, or can only be used for small batch synthesis. Generalized methods for low-cost, low-energy, and ultra-fast synthesis of spinel oxides need to be developed urgently.

A more direct supply of energy to the reaction system through physical conditions is one of the most important means of achieving rapid synthesis [22,23]. Joule heating is a simple method with high energy efficiency which is potential to achieve the purpose of high throughput synthesis. The large amount of Joule heat generated by the instantaneous substrate of a large current through the conductive substrate rapidly supplies energy ($Q = I^2Rt$) to the reaction system, allowing the chemical reaction to be completed in a very short time [24]. The simple device and transient heating characteristics make Joule heating suitable for the production of nano-

* Corresponding authors.
E-mail addresses: lihaixia@nankai.edu.cn (H. Li), yzh@nankai.edu.cn (Z. Yan).

https://doi.org/10.1016/j.cclet.2024.109501
1001-8417/

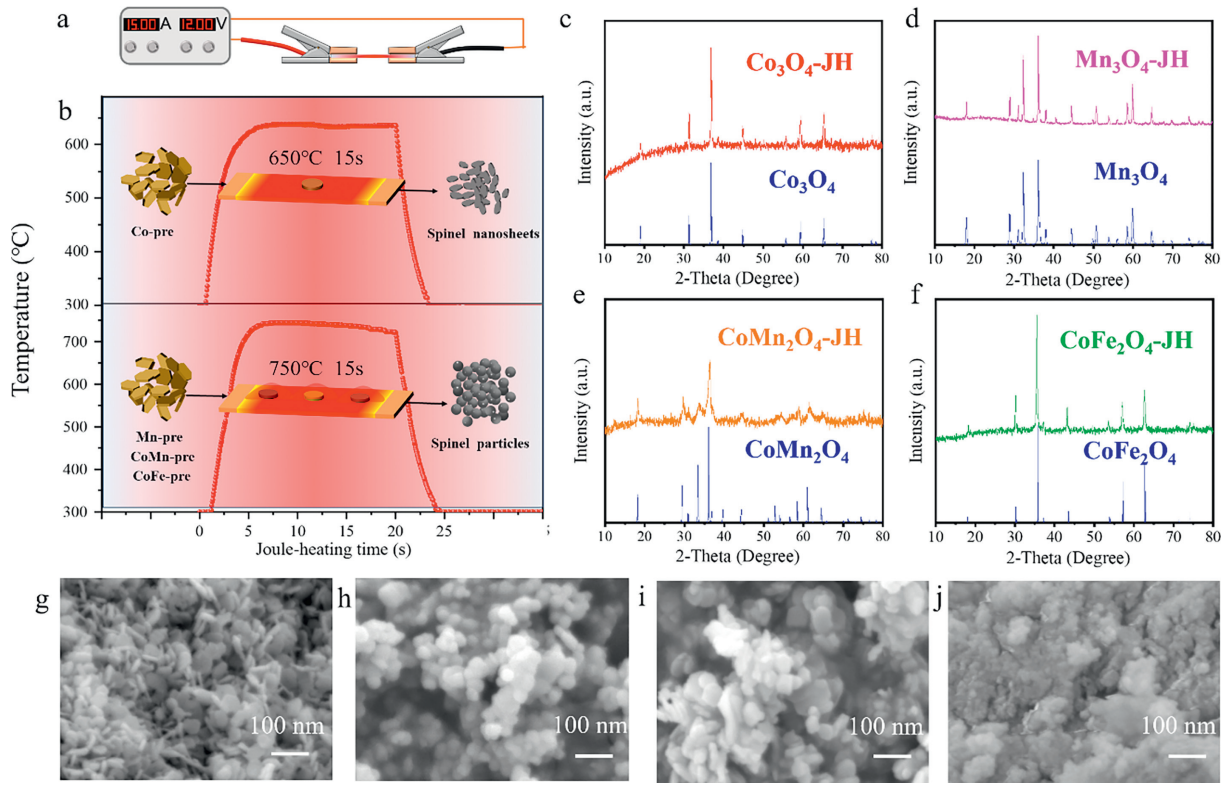

Fig. 1. Schematic diagram of (a) Joule heating equipment. The alligator clip's head is made of electrically conductive copper tape. (b) Joule heating process and temperature-time curves of different precursors. XRD patterns of (c) Co_3O_4–JH, (d) Mn_3O_4–JH, (e) $CoMn_2O_4$–JH and (f) $CoFe_2O_4$–JH. SEM images of (g) Co_3O_4–JH, (h) Mn_3O_4–JH, (i) $CoMn_2O_4$–JH and (j) $CoFe_2O_4$–JH. The scale bar is 100 nm.

micron scale functional materials, such as high entropy alloys [25], high entropy oxides [26,27], oxide lithium cathode materials [28], solid electrolytes [29,30], and it has been extended to the synthesis of small molecules [31]. However, there are few reports on the synthesis of nanocrystalline spinel catalysts by the Joule heating method.

Here we develop a Joule heating method to synthesize various components of spinel oxide materials (Co_3O_4–JH, Mn_3O_4–JH, $CoMn_2O_4$–JH and $CoFe_2O_4$–JH) under the similar condition. We devised an *in-situ* TEM method to simulate the formation process of the spinel phase, revealing that the nanosheets crack into smaller nanosheets or particles due to the exudation of the oxygen, and also determining the effect of the atmosphere and time regulation on the composition and morphology. This Joule heating is an ultrafast (15 s), universal method for synthesizing spinel nanocrystals with good electrocatalytic oxygen reduction performance. Our work expands the application conditions of Joule heating synthesis materials and provides a reference for controlling the morphology of nanocrystals.

To emphasize the universality of our approach, a common precipitation or co-precipitation method was applied to the preparation of precursors, as shown in the Experiment Section, and precursors were named as Co-pre, Mn-pre, CoMn-pre and CoFe-pre according to the transition metal elements contained in the precursor. As illustrated in Fig. 1a, a current controlled by a DC power supply flows through the carbon paper substrate (held by two alligator clips) generating Joule heat, and the temperature of the carbon paper rapidly increase to provide a large amount of energy to the reaction system. After being tableted, a Joule heating process with a setting voltage of 12 V acted on Co-pre, and the product was collected after a sintering temperature of ~650 °C for about 15 s (Fig. 1b). Mn-pre, CoMn-pre and CoFe-pre was calcined at ~750 °C for about 15 s with the setting voltage of 15 V. It is worth emphasizing that Mn-pre, CoMn-pre and CoFe-pre can be calcined at the same time (Fig. S1 in Supporting information). It can be seen in optical photos (Fig. S3 in Supporting information) that the three components were in the same space and did not affect each other before and after synthesis, which reflected the potential of Joule heating method in high throughput synthesis. Carbon paper can be reused according to Fig. S2 (Supporting information). Figs. S2a and b are photos of the carbon paper before and after heating. And the thermal curve (Fig. S2c) of after heating were similar to that of before heating.

Phase information was revealed by X-ray diffraction (XRD). The precursors were oxides and hydroxides (Fig. S6 in Supporting information). Products were named as Co_3O_4–JH, Mn_3O_4–JH, $CoMn_2O_4$–JH and $CoFe_2O_4$–JH. Fig. 1c shows that the final product of Co-pre after Joule heating method was the cubic spinel Co_3O_4 (JCPDS No. 43-1003), and the XRD patterns of the other three products correspond to tetragonal spinel Mn_3O_4 (JCPDS No. 1-1127), tetragonal spinel $CoMn_2O_4$ (JCPDS No. 77-471) and cubic spinel $CoFe_2O_4$ (JCPDS No. 1-1121), respectively (Figs. 1d–f), showing the formation of the most stable phase of the specific temperature condition even in a short duration of heating [32]. Scanning electron microscope (SEM) was used to observe the microscopic surface morphology of the powder samples of precursors and products. As shown in Fig. S5 (Supporting information), four types of precursors were mainly nanosheets, which was the common morphology of transition metal hydroxides. Meanwhile, the appearance of a small number of nano particles can be observed in the SEM image of Mn-pre, indicating the presence of oxides, corresponding to XRD. Co_3O_4 shows a morphology of nanosheets with the size of 100 nm (Fig. 1g), when the others tend to be nanoparticles with the particle size of 30–50 nm (Figs. 1h–j). It is indicated that a higher temperature shock brought a fracture of nanosheets to be nanoparticles and agglomeration in rapid sequence.

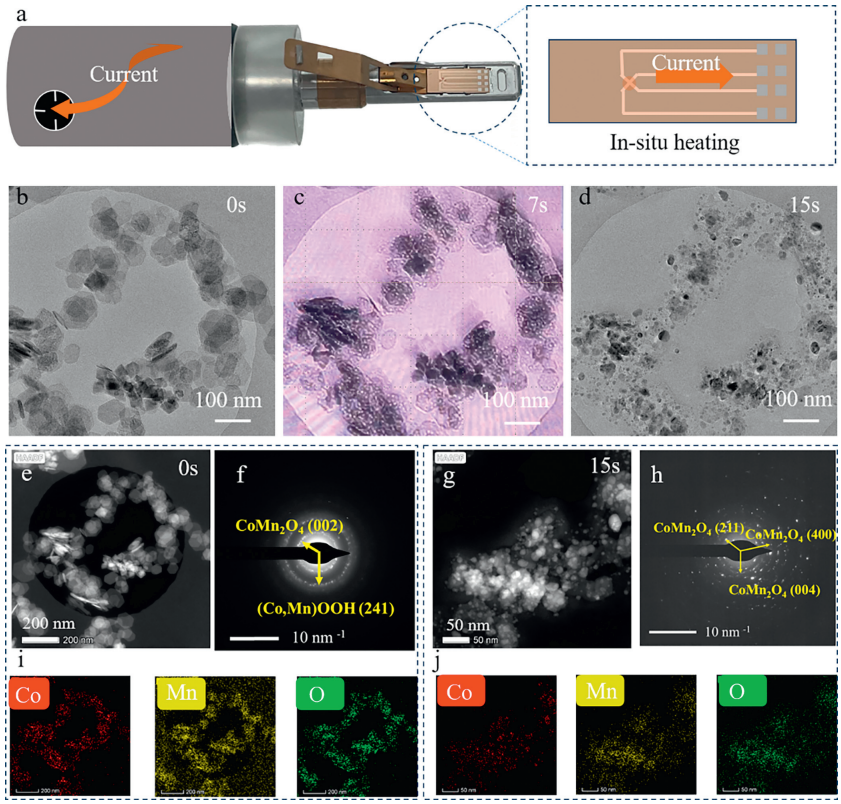

Fig. 2. (a) Schematic diagram of *in-situ* Joule-heating holder and substrate chip. TEM image of the sample at (b) 0 s (c) 7 s and (d) 15 s. The scale bar is 100 nm. (e) HAADF-TEM image of the sample before heating. (f) SAED image of the sample before heating. (g) HAADF-TEM image of the sample after heating. (h) SAED image of the sample after heating. (i) EDS-Mapping of the sample before heating and (j) after heating.

Then, we demonstrate an *in-situ* method to reveal the Joule-heating process. The CoMn-pre powder sample was dispersed into ethanol and dripped onto a silicon–carbon chip with an electric circuit on it. The chip was purchased from ThermoFisher Scientific (Fig. 2a and Fig. S14 in Supporting information), and served as the substrate of TEM samples on the *in-situ* heating sample holder. To simulate the Joule heating process, the sample holder was connected to a programmable power supply (Keithley 2604B), and the entire heating process was controlled by a MEMES-Heater software. Before heating, a TEM image and selective area electron diffraction (SAED) image of CoMn-pre was recorded. As shown in Fig. 2b, CoMn-pre displayed the nanosheet shape, and the SAED patterns in Fig. 2e indicated that the precursor was composed of (Co,Mn)OOH in which the (002) the (241) crystal face of (Co,Mn)OOH can be identified. The HAADF EDS-Mapping showed that in Co, Mn and O were distributed evenly in CoMn-pre (Figs. 2e, f and i). A heating program was set in the MEMS-Heater software, according to the heating curves obtained in the experiment. The heating speed was 150 °C/s, the maximum temperature was set to 750 °C, and the heating program was started subsequently. As recorded in Figs. 2b–d, the nanosheets underwent a crack-break-agglomeration process. The escape of gases during the decomposition reaction led to the formation of many holes on the surface of the nanosheets (Fig. 2c, after 7 s of heating), and the nanosheets cracked upon further heating, eventually forming nanoparticles, with the small particles tending to be enriched towards the larger ones and eventually forming particles with sizes ranging from 10 nm to 50 nm (Figs. 2d and g). Fig. 2h showed SAED images after *in-situ* heating, where the presence of diffraction rings representing the (211), (400), and (004) crystal planes of $CoMn_2O_4$ can be observed, and the distribution of Co, Mn, and O was suggested in Fig. 2j. It indicated that the process of synthesis of spinel by Joule heating of hydroxide precursor was a process in which the escape of oxygen-containing gas leads to the cracking of nanosheet structure, and oxygen vacancy was formed at the cracking edge. If sufficient oxygen elements were not absorbed from the environment, the precipitation of Co would eventually result. On the other hand, we observed the formation and agglomeration of smaller particles in this process, which gave us two implications: First, the synthesis of spinel oxides by Joule heating method needed to be carried out in an air atmosphere, and if the reaction time can be reasonably shortened, there was a chance to obtain smaller nanoparticles. In order to refine the process of Joule thermal decomposition of the lamellar precursor, we performed programmed warming under *in-situ* electron microscopy, and the relevant results are supplemented in Fig. S15 (Supoprting information). We set a heating rate of 150 °C/s and held the temperature for a period of time every 100 °C to record the sample morphology. It can be observed that the nanosheets start to produce holes at 300 °C, the voids are already very dense at 600 °C, and a clear rupture of the nanosheets with the generation of smaller nanosheets and nanoparticles can be observed at 700 °C. By 800 °C, the material has been completely broken into nanoparticles.

Based on the results of *in-situ* transmission electron microscopy, we propose a C-B-A process to describe the phase transition under Joule thermal shock. As shown in Fig. 3a, C represents the thermal decomposition reaction of the precursor under thermal shock, oxygen-containing gas escapes, and continuous heating causes the nanosheet to crack, break (B), and eventually form smaller nanosheets or nanoparticles and aggregate (A). Notably, there are some obvious holes in the nanosheets (Fig. S4a), which indicates a possible process that the decomposition and gas escape of precursors in the Joule heating process cause the nanosheets to break first into smaller nanosheets, then into smaller nanoparticles, and

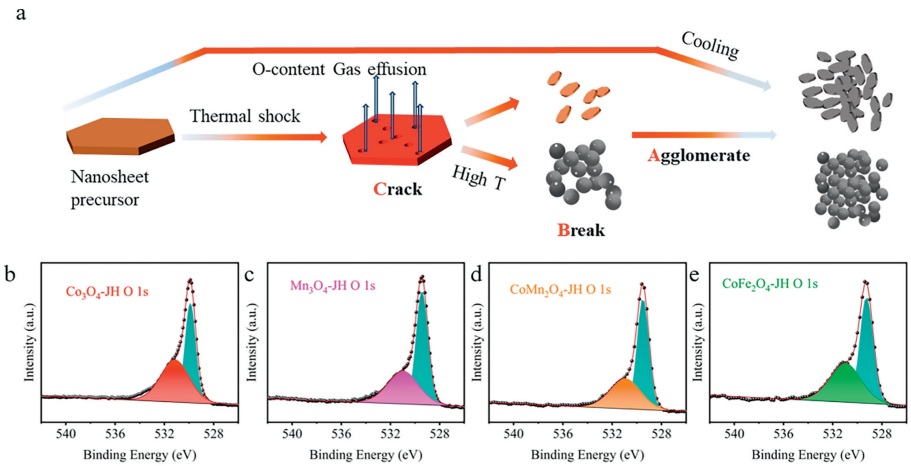

Fig. 3. (a) Schematic diagram of C-B-A process of Joule-heating method. High resolution O 1s spectrum of (b) Co_3O_4–JH, (c) Mn_3O_4–JH, (d) $CoMn_2O_4$–JH and (e) $CoFe_2O_4$–JH.

finally to agglomerate into larger nanoparticles. This decomposition process leads to the formation of O vacancy on the surface of the final nanosheet or nanoparticle, which can be demonstrated by the characterization of X-ray photoelectron spectroscopy (XPS). The full spectrums and high-resolution spectrums of the four products are listed in Figs. S7–S10 (Supporting information). In the high-resolution O 1s spectrum of the four oxides (Figs. 3b–e), the peak of ~531 eV is ascribed to oxygen absorbed on the surface of materials, indicating that the surface tends to absorb oxygen around the environment because of the presence of O vacancy, and generation of O vacancy further might improve the electrocatalytic performance of the materials [33].

High resolution transmission electron microscopy (HRTEM) image and its fast Fourier transform (FFT) was used to observe the lattice fringes and crystal plane spacing clearly. In Figs. S4e and i (Supporting information), two groups of lattice spacing with the width of 0.243 nm are indicated, and their included angle is 84.8°, which can be attributed to the (311) crystal plane and $(1\bar{3}1)$ crystal face of cubic spinel Co_3O_4. Figs. S4f and j (Supporting information) showed (211) and (020) faces of tetragonal spinel Mn_3O_4 with the angle of 64.4°, respectively with the width of 0.248 nm and 0.287 nm. (211) face (0.248 nm) of tetragonal spinel $CoMn_2O_4$, and (311) face (0.253 nm) cubic spinel $CoFe_2O_4$ were calibrated in Figs. S4g, S4k (Supporting information) and Figs. S4h, S4l (Supporting information), respectively. (211) face is the dominant crystal face of tetragonal phase spinel, while (311) is the counterpart of cubic phase spinel. This structural information further confirmed that we had successfully obtained four kinds of spinel oxide products by Joule heating method. Moreover, from these characterization methods, the transformation process of flake hydroxide precursor to spinel oxide after Joule heating can be inferred simply. The escape of water and other gases generated by decomposition from the nanosheet leads to the cracking of the nanosheets, and higher reaction temperature corresponded to greater fragmentation. Under such non-equilibrium transient heating, the surface of small nanosheets or particles produced by decomposition cannot be supplemented with oxygen elements in time, resulting in the formation of surface oxygen vacancies. This indicates that, different from the more perfect crystals produced by the traditional long-term equilibrium heating reaction, the Joule heating method can produce nano-scale crystals with certain defects on the surface with ultrafast and high throughput. The structure-to-performance of defective crystals is also a hot topic in materials science.

The ORR performances of Co_3O_4–JH, Mn_3O_4–JH, $CoMn_2O_4$–JH and $CoFe_2O_4$–JH were first evaluated in an O_2-saturated 0.1 mol/L KOH solution using a rotating ring-disk electrode (RRDE). The catalysts consist of a physical mixture of oxides and conductive carbon before loading on the RRDE electrode with a load of 0.25 mg_{oxide}/cm^2. As shown in cyclic voltammograms (CVs, Fig. 4a and Fig. S13 in Supporting information), all the four catalysts display no reduction peak in an Ar atmosphere while one distinguishable reduction cathodic peak is observed in an O_2 atmosphere, indicating the ORR catalytic capability. ORR polarization curves were further obtained at an electrode rotating rate of 1600 rounds per minute (rpm) and a scan rate of 5 mV/s. In Figs. 4a, b and d, $CoMn_2O_4$-JH exhibited a best ORR performance with an onset potential (E_{onset}) of 0.94 V, a half wave potential ($E_{1/2}$) of 0.79 V and a Tafel slope of 83.9 mV/dec. The $E_{1/2}$ value of Co_3O_4–JH, Mn_3O_4–JH and $CoFe_2O_4$–JH were 0.77, 0.78 and 0.76, respectively. The electron transfer number is acquired by linear sweep voltammograms (LSV) with RRDE at different rotating rates (Fig. S12 in Supporting information), and the electron transfer number of Co_3O_4–JH, Mn_3O_4–JH, $CoMn_2O_4$–JH and $CoFe_2O_4$–JH are 3.62, 2.96, 3.92 and 2.68 at a potential of 0.4 V (Fig. 4c). The ECSA of spinels were calculated by the plot of CVs at different scan rates, and $CoMn_2O_4$–JH had the highest C_{dl} of 5.8 mF/cm^2 (Fig. S11 in Supporting information). Fig. 4e showed the comparison of oxygen reduction catalytic performance of different components of spinel materials. It can be seen that the synthesis of spinel using Joule heating had comparable oxygen reduction performance, which proved that Joule heating is a feasible method for high throughput synthesis.

In summary, we designed a general synthesis method of spinel oxides as oxygen reduction catalysts by a brief precipitation precursor - Joule heating method, products can be calcined on the carbon paper within 15 s. The method we developed has lower time and energy costs compared to traditional methods, according to Table S1 (Supporting information). *In-situ* TEM revealed the changes of morphology and elements with a C-B-A process, and reasonable control of reaction conditions could regulate the oxygen content and particle size of the target products, providing a feasible way to obtain defective oxide nanoparticles. The four kinds of spinel demonstrated by this method had uniform nanomorphology and favorable oxygen reduction performance, among which $CoMn_2O_4$–JH had a half-wave potential of 0.79 V. It is worth mentioning that different components of spinel can be synthesized simultaneously according to the synthesis conditions. The carbon paper used as the substrate can be reused after cleaning with ethanol, also reducing waste. This demonstrates a viable path to develop continuous, high-throughput nano spinel oxides synthesis strategies using Joule heating to further reduce costs and achieve greater market competitiveness.

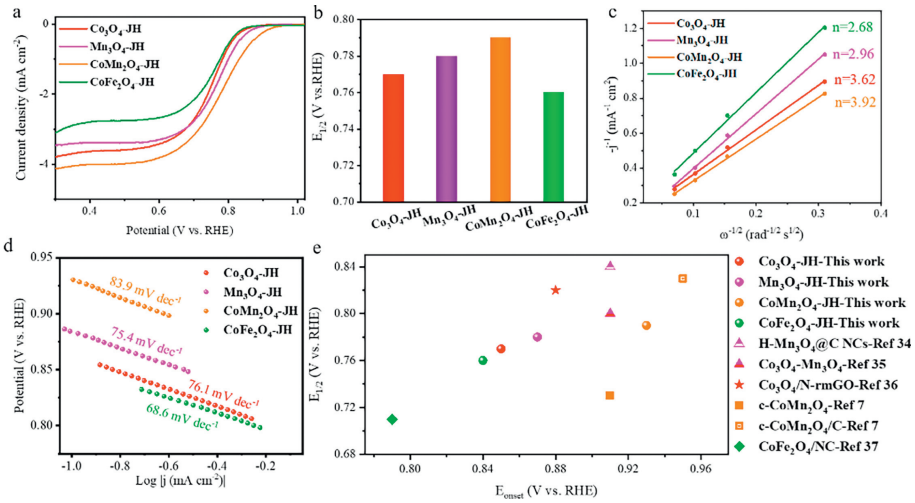

Fig. 4. (a) LSV curves of four spinel oxides synthesized by Joule heating method. (b) The halfwave potential *versus* RHE of spinel products. (c) K-L plot and electron transfer numbers of spinel products. (d) Tafel plot. (e) Comparison of properties of spinel oxygen reduction catalysts in references [7,34–37].

Declaration of competing interest

The authors declare that they have no known competing financial interests or personal relationships that could have appeared to influence the work reported in this paper.

Acknowledgment

This work was supported by the National Programs for Nano-Key Project (No. 2022YFA1504002) the National Natural Science Foundation of China (Nos. 22121005, 22020102002, and 21835004), the Fundamental Research Funds for the Central Universities, and Collaborative Innovation Center of Chemical Science and Engineering (Tianjin).

Supplementary materials

Supplementary material associated with this article can be found, in the online version, at doi:10.1016/j.cclet.2024.109501.

References

[1] H. Xu, J. Yuan, G. He, et al., Coord. Chem. Rev. 475 (2023) 214869.
[2] Q. Zhao, Z. Yan, C. Chen, et al., Chem. Rev. 117 (2017) 10121–10211.
[3] Y. Hao, S.F. Hung, W.J. Zeng, et al., J. Am. Chem. Soc. 145 (2023) 23659–23669.
[4] H. Zhu, S. Zhang, Y.X. Huang, et al., Nano Lett. 13 (2013) 2947–2951.
[5] J. Kim, W. Ko, J.M. Yoo, et al., Adv. Mater. 34 (2022) 2107868.
[6] G. Wu, J. Wang, W. Ding, et al., Angew. Chem. Int. Ed. 55 (2016) 1340–1344.
[7] C. Li, X. Han, F. Cheng, et al., Nat. Commun. 6 (2015) 7345.
[8] X. Wang, M. Yu, X. Feng, eScience 3 (2023) 100141.
[9] C. Wei, Z. Feng, G.G. Scherer, et al., Adv. Mater. 29 (2017) 1606800.
[10] M. Liu, Z. Rong, R. Malik, et al., Energy Environ. Sci. 8 (2015) 964–974.
[11] G. Liang, Z. Wu, C. Didier, et al., Angew. Chem. Int. Ed. 59 (2020) 10594–10602.
[12] L. Shen, L. Yu, X.-Y. Yu, et al., Angew. Chem. Int. Ed. 54 (2015) 1868–1872.
[13] N. Sun, J. Qiu, B. Xu, Adv. Energy Mater. 12 (2022) 2200715.
[14] Y. Wang, Y. Yang, S. Jia, et al., Nat. Commun. 10 (2019) 1506.
[15] M. Prabu, K. Ketpang, S. Shanmugam, Nanoscale 6 (2014) 3173–3181.
[16] X.T. Wang, T. Ouyang, L. Wang, et al., Angew. Chem. Int. Ed. 59 (2020) 6492–6499.
[17] E.M. Davis, A. Bergmann, C. Zhan, et al., Nat. Commun. 14 (2023) 4791.
[18] H. Yang, Y. Liu, X. Liu, et al., eScience 2 (2022) 227–234.
[19] Y. Pei, C.Y. Xu, Y.C. Xiao, et al., Adv. Funct. Mater. 27 (2017) 1604349.
[20] P. Venkateswarlu, E. Umeshbabu, U.N. Kumar, et al., J. Colloid Interface Sci. 503 (2017) 17–27.
[21] L. Lv, Y. Wang, P. Cheng, et al., J. Alloys Compd. 904 (2022) 164054.
[22] D. Yu, Y. Hao, S. Han, et al., ACS Nano 17 (2023) 1701–1712.
[23] Y. Hao, D. Yu, S. Zhu, et al., Energy Environ. Sci. 16 (2023) 1100–1110.
[24] S. Dou, J. Xu, X. Cui, et al., Adv. Energy Mater. 10 (2020) 2001331.
[25] Y. Yao, Z. Huang, P. Xie, et al., Science 359 (2018) 1489–1494.
[26] T. Li, Y. Yao, B.H. Ko, et al., Adv. Funct. Mater. 31 (2021) 2010561.
[27] H. Wu, Q. Lu, Y. Li, et al., Nano Lett. 22 (2022) 6492–6500.
[28] W. Zhu, J. Zhang, J. Luo, et al., Adv. Mater. 35 (2023) 2208974.
[29] M. Hong, Q. Dong, H. Xie, et al., ACS Energy Lett. 6 (2021) 3753–3760.
[30] R. Wang, Q. Dong, C. Wang, et al., Adv. Mater. 33 (2021) e2100726.
[31] Q. Dong, Y. Yao, S. Cheng, et al., Nature 605 (2022) 470–476.
[32] F. Cheng, J. Shen, B. Peng, et al., Nat. Chem. 3 (2011) 79–84.
[33] H. Huang, A. Huang, D. Liu, et al., Adv. Mater. 35 (2023) 2303109.
[34] T. Li, B. Xue, B. Wang, et al., J. Am. Chem. Soc. 139 (2017) 12133–12136.
[35] L. Dai, M. Liu, Y. Song, et al., Nano Energy 27 (2016) 185–195.
[36] Y. Liang, Y. Li, H. Wang, et al., Nat. Mater. 10 (2011) 780–786.
[37] Y. Go, K. Min, H. An, et al., Chem. Eng. J. 448 (2022) 137665.